atmosphere

Article

Characteristics of Particle Size Distributions of Falling Volcanic Ash Measured by Optical Disdrometers at the Sakurajima Volcano, Japan

Masayuki Maki [1,*], Ren Takaoka [2] and Masato Iguchi [3]

1 Research and Education Center for Natural Hazards, Kagoshima University, Kagoshima 890-0065, Japan
2 Graduate School of Science and Engineering, Kagoshima University, Kagoshima 890-0065, Japan; k6636104@kadai.jp
3 Disaster Prevention Research Institute, Kyoto University, Kyoto 611-0011, Japan; iguchi.masato.8m@kyoto-u.ac.jp
* Correspondence: maki@gm.kagoshima-u.ac.jp

Abstract: In the present study, we analyzed the particle size distribution (PSD) of falling volcanic ash particles measured using optical disdrometers during six explosive eruptions of the Sakurajima volcano in Kagoshima Prefecture, Japan. Assuming the gamma PSD model, which is commonly used in radar meteorology, we examined the relationships between each of the gamma PSD parameters (the intercept parameter, the slope parameter, and the shape parameter) calculated by the complete moment method. It was shown that there were good correlations between each of the gamma PSD parameters, which might be one of the characteristics of falling volcanic ash particles. We found from the normalized gamma PSD analysis that the normalized intercept parameter and mass-weighted mean diameter are suitable for estimating the ash fall rate. We also derived empirical power law relationships between pairs of integrated PSD parameters: the ash fall rate, the volcanic ash mass concentration, the reflectivity factor, and the total number of ash particles per unit volume. The results of the present study provide essential information for studying microphysical processes in volcanic ash clouds, developing a method for quantitative ash fall estimation using weather radar, and improving ash transport and sedimentation models.

Keywords: disdrometer; eruption cloud; fall velocity; gamma function; particle size distribution; quantitative ash fall estimation; Sakurajima; volcanic ash; weather radar

check for updates

Citation: Maki, M.; Takaoka, R.; Iguchi, M. Characteristics of Particle Size Distributions of Falling Volcanic Ash Measured by Optical Disdrometers at the Sakurajima Volcano, Japan. *Atmosphere* **2021**, *12*, 601. https://doi.org/10.3390/atmos12050601

Academic Editors: Meelis Zidikheri and Lars Hoffman

Received: 5 February 2021
Accepted: 21 April 2021
Published: 6 May 2021

1. Introduction

The physical properties and chemical components of ash particles emitted by explosive volcanic eruptions represent useful basic data for investigating the mode, scale, and mechanisms of eruptions. Previous studies have investigated the generation mechanism of individual eruptions [1,2] and the fragmentation process during explosive eruptions by estimating the total grain size distribution following sediment surveys [3–5].

In recent years, volcanic sediment data analysis has facilitated many types of research, such as the detection, tracking, and prediction of ash fall to prevent volcanic disasters [6–8], estimation of the content fraction of particles smaller than 63 µm (which affect aircraft operation) from total grain size distribution [7], and investigation of variation in tephra features with distance from the volcano crater using the 100-year eruption records of volcanoes along the western coast of North America [8].

Although investigating ground sediments deposited following volcanic eruptions is an important method in volcanology research, and for volcanic disaster prevention, sediment data acquired on the ground are inevitably time-integrated, they are usually accumulated hours or days after an eruption. Large historical eruptions have resulted in centuries of accumulated sediment. Conventional geological methods for investigating sediments are limited in that the properties and sedimentary environment of volcanic ash particles change depending on weather conditions, such as wind and rain, during and after sedimentation [9], such that sediment data are often unsuitable for remote sensing and numerical forecasting of ash fall distribution and transportation, which change from moment to moment.

Recent studies have attempted to clarify the physical properties of ash particles at high temporal resolution using meteorological optical disdrometers, which were developed to measure the physical characteristics of precipitation particles [10–12] including particle size distribution (PSD), shape, falling velocity, and canting. Optical disdrometers have also been used to study microphysics in precipitation clouds, to develop quantitative precipitation estimates, and to provide ground truth data for satellite remote sensing of precipitation. Because the optical disdrometer is a non-contact sensor, it can measure falling volcanic ash particles without altering local environmental conditions. A certain type of optical disdrometer can acquire the shape of a falling single particle using its fast scanning frequency, which is typically a few thousands per second.

Free-fall experiments conducted in a large experimental facility measured the falling velocity, shape, and canting angles of ash particles using a two-dimensional video disdrometer (2DVD) [10], which was developed to observe precipitation particles [13,14]. Another type of optical disdrometer, Parsivel^2 [15,16], was installed on Sakurajima, a volcano in Kagoshima Prefecture, Japan to automatically measure falling ash particles [11]. This instrument measured temporal changes in the PSD and fall velocity of tephra from a total of 76 eruptions of Sakurajima over a 2-year period. An analysis of these records showed that temporal changes in the Parsivel^2 PSD data were synchronized with the crustal movements associated with eruptions. Based on the success mentioned above, automated measurements of ash particles are ongoing with 13 Parsivel^2 instruments that have been arranged in all directions centering on the Minami-dake summit of Sakurajima [12].

The goal of the present study was to find characteristics of volcanic ash PSD. One of the unique features of the present study is an analysis of PSD data measured by disdrometers every 1 min. The results obtained will be useful for the radar monitoring of ash falls and improvement of volcanic ash transport and diffusion models.

The structure of the present paper is as follows. In Section 2, we describe the principles by which ash particles are measured by Parsivel^2, the data analysis, and processing methods. In Section 3, we describe the functional forms and integrated parameters of ash particle PSD, which provide a theoretical basis for quantitative ash fall estimation and analysis of volcanic ash cloud microphysics. Our results are described and discussed in Sections 4 and 5, respectively. The phenomenon of fragmentation, which is an important eruption mechanism based on the physical and chemical characteristics of volcanic ash particles, is beyond the scope of this study, and will not be discussed.

2. Measurements of Volcanic Ash Particles

2.1. Parsivel^2

In this study, we used the Parsivel^2 (PARticle SIze and VELocity) optical disdrometer; its main specifications are listed in Table 1 [17]. Parsivel^2 measures falling particles as follows. A flat, horizontal laser measuring surface (180 mm × 30 mm × 1 mm) is formed between the light-emitting and light-receiving devices. The diameter (0.2–25 mm) and fall speed (up to 20 ms^{-1}) of the particles are calculated in real time based on the voltage drop and duration as falling particles pass through the laser measurement surface (Figure 1). In these calculations, it was assumed that particles < 1 mm in diameter are spherical, the axial ratio of particles 1–5 mm in diameter varies linearly from 1 to 0.7, and the axial ratio of particles > 5 mm in diameter is 0.7. These assumptions are based on the original function of Parsivel, which was designed to measure raindrops, and may lead to errors in measurements of volcanic ash particles. At present, it is difficult to estimate these errors because the relationship between the axis ratio and diameter of volcanic ash particles is unclear.

Table 1. Main specifications of the Parsivel^2 disdrometer, according to the instruction manual (OTT, 2011).

Category	Subcategory	Specification
Sensor	Type Wavelength Output rating Laser class	Laser diode 650 nm 0.2 mW 1 (IEC/EN 60825-1: 2014)
Sampling	Light strip (W × D) Area (W × D) Interval	30 × 1 mm (54 cm^2) 180 × 30 mm (54 cm^2) 10 s to 60 min
Output	Particle size Fall velocity Precipitation intensity (accuracy) Precipitation type Radar reflectivity factor Kinetic energy Visibility in precipitation	32 classes: 0.2, . . . , 8 mm (liquid particles) 32 classes: 0.2, . . . , 25 mm (solid particles) 32 classes: 0.2, . . . , 20 m s^{-1} 0.001, . . . , 1200 mm h^{-1} (±5% for liquid, ±20% for solid) 8 types (drizzle, drizzle/rain, rain, snow, mixed rain/snow, snow grains, sleet, hail) −9.999, . . . , 99.999 dBZ ± 20% 0, . . . , 999.999 J/(m^2 h) 0, . . . , 20,000 m

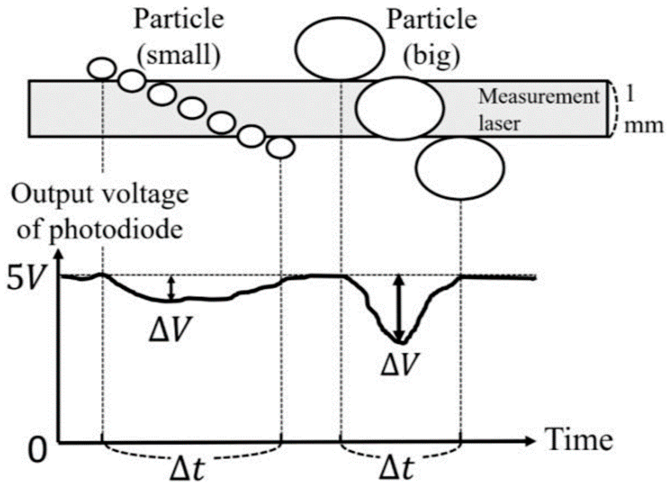

Figure 1. Schematic diagram illustrating ash particle diameter and fall velocity measurements by Parsivel^2 (Löffler-Mang and Joss, 2000). As a particle passes through the measurement laser beam sheet, voltage reduction ΔV is generated during time interval Δt at the light-receiving device. The particle diameter is estimated from ΔV, and fall velocity is estimated from Δt.

The PSD estimation error for Parsivel has been compared with that for other instruments [15,16,18–20]. The accuracy of the first-generation Parsivel and Parsivel^2 was evaluated by comparing measured data with those from an impact disdrometer observing raindrops [16,21]. The results showed that Parsivel^2 has improved the accuracy of rainfall and PSD measurements of particles 0.5 and 4 mm in size. The accuracy of Parsivel^2 is acceptable for estimating the fall velocity of particles < 1 mm in diameter. Parsivel^2 was found to underestimate fall velocity near 1 m s^{-1}, but this trend decreased as particle size increased.

2.2. Data Collection

The ash particle data analyzed in this study were collected by the Parsivel^2 network (Figure 2), which was installed on Sakurajima and operated by the Disaster Prevention Research Institute of Kyoto University. We extracted PSD data, including eruption onset time and cloud top height, from the Parsivel^2 database for six volcanic eruptions that occurred in 2018 (Table 2), according to reports of Sakurajima volcanic eruptions published by the Kagoshima Local Meteorological Observatory of the Japan Meteorological Agency [22,23].

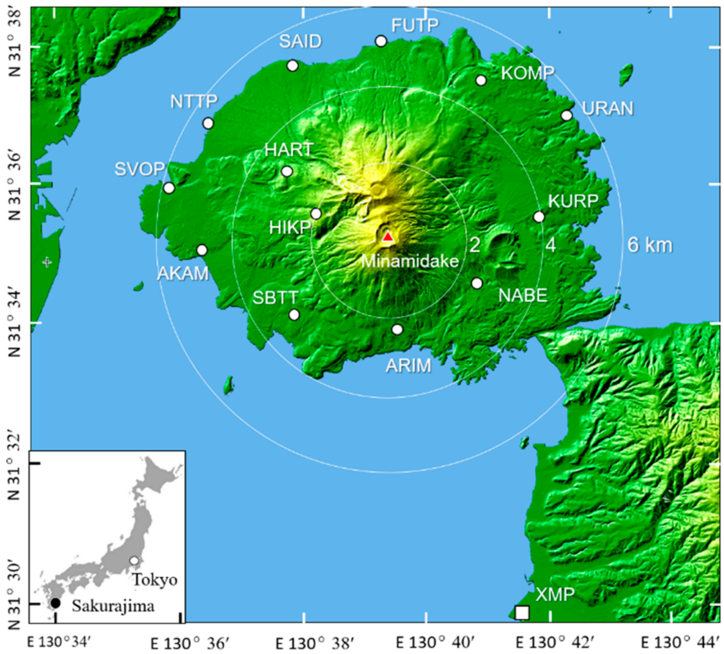

Figure 2. The network of 13 Parsivel^2 instruments installed on Sakurajima to measure volcanic ash particle size distribution (PSD). Triangle indicates the southern summit (Minami-dake); square indicates the position of X-band multi-parameter radar (XMP).

Table 2. List of Sakurajima volcanic eruptions analyzed in the present study.

Case	Eruption Onset (LST)	Cloud Top Height (m)	Movement	Disdrometer Code
1	08:08, 15 May 2018	2500	Top	NABE
2	19:48, 22 May 2018	Unknown	Unknown	HIKP, HART
3	08:01, 30 May 2018	2500	Eastward	KURP
4	11:35, 10 June 2018	3500	Top	HART
5	07:19, 16 June 2018	4700	Westward	SBTT
6	15:38, 16 July 2018	4600	Westward	AKAM

To confirm that an eruption cloud had passed over a Parsivel^2 site, we used X-band multi-parameter radar (XMP), which was installed approximately 11 km from Sakurajima's Minami-dake summit. XMP is operated by the Ministry of Land, Infrastructure and Transport to monitor debris flows on Sakurajima; although it is used to observe precipitation, it has also been shown to capture ash particles falling from eruption clouds [24].

Eruption cases were selected for analysis as follows. First, eruptions in which the eruption cloud top height was >2000 m above the vent were extracted. Then, XMP data for the extracted eruptions were downloaded from the Extended Rainfall Indicator Network (XRAIN) data download system [25] to draw time-cumulative plan position indicator (PPI) images of reflectivity at 2 elevation angles, of 1.7° and 6°. Finally, eruptions in which the installation point of Parsivel^2 was within the cumulative reflectivity distribution area were selected for analysis.

2.3. Data Processing

Various physical quantities of particles falling through the atmosphere were calculated from PSD data measured by Parsivel[2] [26]. The PSD of falling particles is calculated as follows:

$$N(D_i) = \sum_{j=1}^{nd} \frac{C_{ij}}{A_i \cdot \Delta t \cdot V_j \cdot \Delta D_i}; \quad N(D_i)\,[\mathrm{mm^{-1} m^{-3}}],\, D_i[\mathrm{mm}] \tag{1}$$

where $N(D_\mathrm{i})$ is the number of particles from D_i to D_i + ΔD_i in a unit volume, and D_i, ΔD_i are the average and bin spacing of the *i*-th size bin, respectively. C_ij is the number of particles measured in the *i*-th size bin and the *j*-th speed bin, and *nd* is the number of size bins (32 in this study). V_j is the measured time interval (60 s for this instrument), and A_i is the fall rate measured for the *j*-th speed bin. The effective measurement area of the *i*-th size bin is calculated as follows:

$$A_\mathrm{i} = [180 \times (30 - 0.5D_i)] \times 10^{-6} \quad [\mathrm{m^2}] \tag{2}$$

The mean fall velocity of particles with a mean diameter D_i is calculated as follows:

$$V(D_\mathrm{i}) = \sum_{j=1}^{nv} V_j \cdot C_{ij} / \sum_{j=1}^{nv} C_{ij} \quad [\mathrm{m\,s^{-1}}] \tag{3}$$

where *nv* is the number of velocity bins (32 for this instrument). The ash fall rate R_A was calculated as follows:

$$R_\mathrm{A} = \frac{\pi \rho_\mathrm{P}}{6} \sum_{i=1}^{nd} (V(D_i) \cdot N(D_i) \cdot D_i^3); \quad R_\mathrm{A}\,[\mathrm{kg\,m^{-2} s^{-1}}] \tag{4}$$

where ρ_P is the solid density of ash particles. We assumed that ρ_P = 2.5 g cm^{-3} (= 2.5 × 10^3 kg m^{-3}). From Equation (1),

$$R_\mathrm{A} = \frac{\pi}{6} 10^{-9} \rho_\mathrm{P} \sum_{i=1}^{nd} \sum_{j=1}^{nv} D_i^3 \frac{C_{ij}}{A_i\,\Delta t}; \quad R_\mathrm{A}\,[\mathrm{kg\,m^{-2} s^{-1}}] \tag{5}$$

If R_A is expressed in [mm h^{-1}],

$$R_\mathrm{A} = 6\pi\, 10^{-4} \frac{\rho_\mathrm{P}}{\rho_\mathrm{b}} \sum_{i=1}^{nd} \sum_{j=1}^{nv} D_i^3 \frac{C_{ij}}{A_i\,\Delta t}; \quad R_\mathrm{A}\,[\mathrm{mm\,h^{-1}}] \tag{6}$$

where ρ_b is the bulk density of ash deposits. We assumed that ρ_b = 1.25 g cm^{-3} (= 1.25 × 10^3 kg m^{-3}). The volcanic ash mass concentration C_A is defined as the amount of ash particles in a unit volume of air, is calculated as follows:

$$C_\mathrm{A} = \frac{\pi}{6} 10^{-6} \rho_\mathrm{P} \sum_{i=1}^{nd} \sum_{j=1}^{nv} D_i^3 \frac{C_{ij}}{A_i\,\Delta t\, V_j}; \quad C_\mathrm{A}\,[\mathrm{kg\,m^{-3}}] \tag{7}$$

and the reflectivity factor Z is calculated as follows:

$$Z = \sum_{i=1}^{nd} \sum_{j=1}^{nv} D_i^6 \frac{C_{ij}}{A_i\,\Delta t\, V_j}; \quad Z\,[\mathrm{mm^6 m^{-3}}] \tag{8}$$

The mass-weighted diameter D_m is a parameter characterizing the normalized PSD, and is calculated as the ratio of the fourth moment of PSD to the third moment, as follows:

$$D_m = \frac{\sum_{i=1}^{nd} N(D_i) D_i^4 \Delta D_i}{\sum_{i=1}^{nd} N(D_i) D_i^3 \Delta D_i}; \; D_m \text{ [mm]} \tag{9}$$

D_m is closely related to the median volume particle diameter D_0 (Sections 3.2 and 3.4). The normalized PSD intercept parameter N_w is calculated as follows:

$$N_w = \frac{4^4}{\pi \rho_p} \left[\frac{C_A}{D_m^4} \right]; \; N_w \text{ [mm}^{-1}\text{m}^{-3}] \tag{10}$$

The basic parameters of volcanic ash particles described above were directly calculated from PSD data measured by Parsivel^2.

3. Functional Representation of Falling Ash Particles

3.1. Radar Meteorological Approach

In radar meteorology, precipitation PSD is indispensable for quantitative estimation of precipitation and hydrometeor classification. Therefore, functions to approximate observed precipitation particles have been proposed in several previous studies. Functional forms of PSD can be used to investigate spatiotemporal variation in the microphysical processes of precipitation clouds, derive theoretical formulae for quantitative precipitation estimates, and simulate precipitation particle scattering.

In this study, we applied radar meteorology concepts and techniques to volcanic ash fall phenomena. In this section, we describe volcanic ash PSD using either gamma or normalized gamma functions. In addition, we show that the integrated PSD parameters such as R_A, C_A, Z, etc. can be expressed in terms of either gamma or normalized gamma PSD models.

3.2. Gamma PSD Model

Raindrop size distribution is commonly described using the gamma PSD model. In this study, we replaced raindrops with falling ash particles in the gamma PSD model, which is expressed as follows [27,28]:

$$N(D) = N_0 D^{\mu} \exp(-\Lambda D) \tag{11}$$

where $N(D)$ is the number of ash particles per unit diameter increment within a unit volume, N_0 (mm$^{-1-\mu}$ m^{-3}) is the intercept parameter characterizing PSD, Λ (mm^{-1}) is the slope parameter, and μ is the shape parameter. D is expressed in mm, and μ, which is normally dimensionless, takes the units of N_0. Thus, N_0 and μ are not completely independent, such that N_0 is affected by the variation of μ and N_0 has no physical meaning [29]. Equation (11) can be expressed using the median volume diameter D_0, which has a physical meaning and is used in radar meteorology instead of Λ. Thus,

$$N(D) = N_0 D^{\mu} \exp[-G(D/D_0)] \tag{12}$$

When $D_{max}/D_0 \geq 2.5$, and $\mu \geq -3$, the following approximation holds, with an accuracy of $\leq$0.5% [27]: $G = \Lambda D_0 = 3.67 + \mu$. The median volume diameter D_0 is defined as the diameter that divides the total volume of all falling ash particles within a unit volume into two equal parts in the falling ash PSD. Since the computation of D_0 is cumbersome, the mass-weighted mean D_m is often used instead of D_0. The relationship between D_m and D_0 is as follows [27]:

$$D_m = (4 + \mu)/(3.82 + \mu) D_0 \tag{13}$$

The value 3.82 in the above equation is attributed to a power law approximation of the fall velocity of ash particles ($D \leq 2$ mm; Table 3). The value 3.67 is typically used for raindrops. From Equation (13), when $\mu \geq 0$, the difference between D_m and D_0 is less than 9%, and as μ becomes larger, this difference becomes smaller; when μ = 10, the difference is about 2%. Using D_m to represent the gamma PSD, the model becomes:

$$N(D) = N_0 D^{\mu} \exp[-(4+\mu)(D/D_m)] \quad (14)$$

The intercept parameter Λ can be expressed as follows:

$$\Lambda = (4+\mu)/D_m \quad (15)$$

As a special case of the gamma distribution, μ = 0,

$$N(D) = N_0 \exp(-\Lambda D) = N_0 \exp[-G(D/D_0)] \quad (16)$$

or

$$N(D) = N_0 \exp[-4(D/D_m)] \quad (17)$$

This PSD model is a well-known exponential PSD function [30].

Table 3. List of coefficients and exponents of ash particle fall velocity formulae proposed in previous studies. V_t (D) = a D^b, where V_t is expressed in m s^{-1} and D is expressed in mm.

a	*b*	Note	Reference
5.90	0.530	0.25 ≤ D < 4 mm (free fall experiments, Parsivel^2)	Miwa et al. [31]
5.96	0.530	0.25 ≤ D < 4 mm (free fall experiments, 2DVD)	Suh et al. [10]
4.04	0.830	0.25 ≤ D < 2 mm (Sakurajima, Parsivel^2, 26,075 particles)	Kozono et al. [32]
3.96	0.748	0.25 ≤ D < 4 mm (Sakurajima, Parsivel^2, 79,170 particles)	Kozono [33]
3.18	0.728	0.25 ≤ D < 4 mm (Sakurajima, Parsivel^2, 63,237 particles)	Present study
3.14	0.817	0.25 ≤ D < 2 mm (Sakurajima, Parsivel^2, 63,237 particles)	Present study
3.42	0.371	0.2 ≤ D ≤ 6.0 mm (Mt. St. Helens, 19 March 1982)	Harris and Rose [34]
5.02	0.335	0.22 ≤ D ≤ 1.3 mm (Mt. St. Helens, 19 March 1982)	Harris and Rose [34]
6.87	1.0	0.02 ≤ D ≤ 0.38 mm (Mt. St. Helens, 18 May 1980)	Harris and Rose [34]
4.33	0.437	0.02 ≤ D ≤ 6.0 mm (Mt. St. Helens, all data)	Present study (average)

3.3. Normalized Gamma PSD Model

Generally, falling ash PSDs fluctuate depending on C_A or R_A. To investigate the shape of the ash PSD, which is not affected by C_A, normalized (scaled) PSD concepts have been proposed [35–40]. The normalized PSD is generally expressed as follows [39]:

$$N(D) = N_w F(D/D_m) = N_w F(X) \quad (18)$$

where N_w is the normalized intercept parameter, which normalizes N (D), and D_m is the mass-weighted mean diameter, which normalizes D. F is a factor that determines the geometry of the PSD, and $X = D/D_m$. The normalized PSD expressed in Equation (18) is not a functional form of PSD. In this section, we derive a normalized PSD assuming a gamma function for measured PSD.

When $N(D)$ is represented by the gamma function, i.e., Equation (12), the nth moment M_n of PSD is expressed as follows:

$$M_n = \int_0^{\infty} D^n N(D) dD = \frac{N_0 \Gamma(n+1+\mu)}{\Lambda^{n+\mu+1}} \quad (19)$$

D_m and N_w are expressed as follows, in terms of M_n:

$$D_m = M_4/M_3 = (4+\mu)/\Lambda \tag{20}$$

$$N_w = \frac{4^4}{\Gamma(4)}\frac{M_3^5}{M_4^4} = N_0 D_m^{\mu}\frac{\Gamma(4+\mu)}{\Gamma(4)}\frac{4^4}{(4+\mu)^{4+\mu}} \tag{21}$$

From Equations (14), (18), (20), and (21),

$$F(X) = \frac{\Gamma(4)}{4^4}\frac{(4+\mu)^{4+\mu}}{\Gamma(4+\mu)}X^{\mu}\exp[-(4+\mu)X] \tag{22}$$

Therefore, the normalized gamma PSD can be represented as follows:

$$\frac{N(D)}{N_w} = \frac{\Gamma(4)}{4^4}\frac{(4+\mu)^{4+\mu}}{\Gamma(4+\mu)}\left(\frac{D}{D_m}\right)^{\mu}\exp[-(4+\mu)\left(\frac{D}{D_m}\right)] \tag{23}$$

Importantly, the normalized gamma PSD described in Equation (23) is represented by three independent parameters, N_w, D_m, and μ.

3.4. Calculation of PSD Parameters

Three parameters of the gamma PSD, N_0 (or N_w), Λ (D_0 or D_m), and μ can be calculated using the nth moment M_n of the PSD [41,42], as follows:

$$M_n = \int_0^{\infty} D^n N(D)dD \tag{24}$$

M_n can be calculated by the following equation using PSDs measured by Parsivel^2:

$$M_n = \sum_{i=1}^{32} D_i^n N_i(D_i) \tag{25}$$

For convenience of computation, we introduce a variable η, which is defined as the combination of M_2, M_4, and M_6, as follows:

$$\eta = \frac{M_4^2}{M_2 M_6} = \frac{[\Gamma(5+\mu)]^2}{\Gamma(3+\mu)\Gamma(7+\mu)} = \frac{(3+\mu)(4+\mu)}{(5+\mu)(6+\mu)}. \tag{26}$$

such that η is a monotonically increasing function with respect to μ. By solving Equation (26), the shape parameter μ of the gamma PSD model can be obtained from the following equation:

$$\mu = \frac{(7-11\eta) - (\eta^2 + 14\eta + 1)^{1/2}}{2(\eta - 1)}. \tag{27}$$

If μ is known, the slope parameter Λ of the gamma profile is given by [42]:

$$\Lambda = \left[\frac{M_2\Gamma(5+\mu)}{M_4\Gamma(3+\mu)}\right]^{1/2} = \left[\frac{M_2(4+\mu)(3+\mu)}{M_4}\right]^{1/2} \tag{28}$$

where $\Gamma(x) = (x-1)\Gamma(x-1)$. N_0 is calculated as follows:

$$N_0 = \frac{M_n\Lambda^{\mu+n+1}}{\Gamma(\mu+n+1)} \quad (n = 2, 4, \text{ or } 6) \tag{29}$$

where N_0 can be obtained by specifying any value of n if μ and Λ are obtained. Thus, n can be 2, 4, or 6, and the difference in the calculated value of N_0 for each case is about 1%. D_0 can be computed as follows if μ and Λ are obtained:

$$D_0 = \frac{3.82 + \mu}{\Lambda} \tag{30}$$

The present paper utilizes the complete moment method to calculate the gamma PSD parameters. However, it may be necessary to mention that the calculation of gamma PSD parameters is more complex than the complete moment method when the lower and upper bounds of the integral are finite in Equation (24), i.e., an incomplete gamma distribution. The effects of $D_{\rm min}$ and $D_{\rm max}$ on the calculated gamma PSD parameters have been examined assuming an incomplete gamma distribution [42]; the effect of $D_{\rm min}$ on the gamma PSD parameters is small, such that $D_{\rm min}$ = 0 may be assumed [43,44]. The present paper use the observed $D_{\rm max}$ to estimate the nth moment of the PSD.

3.5. Integrated PSD Parameters

The integrated PSD parameters include the total number of falling ash particles $N_{\rm T}$, $C_{\rm A}$, $R_{\rm A}$, and Z. The integrated parameters are expressed by PSD moments, as follows:

$$N_{\rm T} = \int_0^{D_{\rm max}} N(D)dD = m_0 \tag{31}$$

$$C_{\rm A} = \frac{\rho_w \pi}{6} \int_0^{D_{\rm max}} D^3 N(D)dD = \frac{\rho_w \pi}{6} m_3 \tag{32}$$

$$\begin{aligned} R_{\rm A} &= \tfrac{\rho_w \pi}{6} \int_0^{D_{\rm max}} D^3 v_{\rm t}(D) N(D)dD \\ &= \tfrac{a\rho_w \pi}{6} \int_0^{D_{\rm max}} D^{3+b} N(D)dD = \tfrac{\rho_w \pi}{6} m_{3+b} \end{aligned} \tag{33}$$

where $v(D)$ is the falling velocity of volcanic ash particles of diameter D, calculated as follows:

$$v_{\rm t}(D) = aD^b \tag{34}$$

$$Z = \int_0^{D_{\rm max}} D^6 N(D)dD = m_6 \tag{35}$$

The integrated PSD parameters defined in Equations (31)–(33) are determined by PSD moments calculated from the measured PSD data, and the relationships among integrated PSD parameters can be obtained by regression analyses of the integrated PSD parameters. If the PSD data are not available, then the relationships among integrated PSD parameters are derived by assuming the functional form of the PSD. Assuming the gamma PSD model, the following relationships are derived:

$$N_{\rm T} = m_0 = \frac{N_0}{\Lambda^{\mu+1}} \gamma\left(\mu + 1, \alpha \frac{D_{\rm max}}{D_{\rm m}}\right) \tag{36}$$

$$C_{\rm A} = \frac{\rho_w \pi}{6} m_3 = \frac{\rho_w \pi}{6} \frac{N_0}{\Lambda^{\mu+4}} \gamma\left(\mu + 4, \alpha \frac{D_{\rm max}}{D_{\rm m}}\right) \tag{37}$$

$$R_{\rm A} = \frac{\rho_w \pi}{6} m_{3+b} = \frac{\rho_w \pi}{6} \frac{N_0}{\Lambda^{\mu+b+4}} \gamma\left(\mu + b + 4, \alpha \frac{D_{\rm max}}{D_{\rm m}}\right) \tag{38}$$

$$Z = m_6 = \frac{N_0}{\Lambda^{\mu+7}} \gamma\left(\mu + 7, \alpha \frac{D_{\rm max}}{D_{\rm m}}\right) \tag{39}$$

The gamma PSD parameters obtained by the full moment method in Section 3.4 may then be substituted into these equations.

4. Results

4.1. Fall Speed of Volcanic Ash Particles

The terminal velocity of falling particles is generally determined according to the balance among gravitational, buoyancy, and aerodynamic drag forces [45]. In the present study, we express the particle fall velocity as a power law function of particle diameter, as shown in Equation (33), which is obtained by applying regression analysis to fall velocity data measured using Parsivel^2, as shown in Equation (3).

The distribution of the number of ash particles in the parameter space of fall velocity and diameter for the six selected volcanic eruptions is shown in Figure 3. The total number of samples was 63,237, and most of the observed data were for ash particles, i.e., $D \leq 2$ mm. Particles with diameters ranging from 0.4 to 0.8 mm were the most frequent. The fall velocities corresponding to these particles were widely distributed, from 0.2 to 4 ms^{-1}, with larger particles occurring less frequently but with greater variance. This variation may be caused by Parsivel^2 measurement error or particle density variation. The falling velocity of particles increased in proportion to the square of the particle density [45]. Another reason for the large scatter observed in Figure 3 may be the particle shape, which determines the drag force acting on the particle [10]. The flatter the particle shape, the slower the falling velocity.

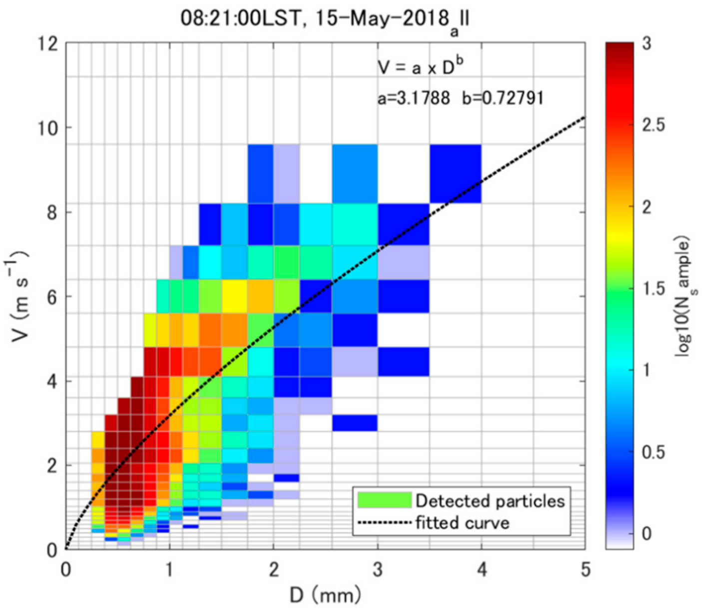

Figure 3. Density plots of the particle size and fall velocity of volcanic ash particles for six selected eruptions of the Sakurajima volcano. Data were collected by Parsivel^2. Color scale indicates drop counts on a log scale. Line indicates the regression curve based on a power law.

The largest particle observed in the present study was 4 mm in diameter. The power law equation for the fall velocity of all data shown in Figure 3 is:

$$v_t = 3.18D^{0.728};\ v_t\,[\mathrm{ms^{-1}}],\ D\,[\mathrm{mm}] \tag{40}$$

For volcanic ash particles ($D \leq 2$ mm), the fall velocity equation is:

$$v_t = 3.14D^{0.817};\ v_t\,[\mathrm{ms^{-1}}],\ D\,[\mathrm{mm}] \tag{41}$$

which is quite similar to Equation (40).

Table 3 summarizes the fall velocity equation derived in the present study and those proposed in previous studies. The equations for fall velocity versus diameter listed in Table 3 are shown in Figure 4. Among all curves shown in Figure 4, the formulae derived from experiments of ash particle free fall from a height of 17 m [10,31] give the largest fall velocity for the same diameter, likely because the fall velocity was accelerated by the fingering phenomenon [46,47]. Parsivel^2, installed on Sakurajima, was used to observe the falling velocity of actual ash particles. [11,32]; the falling velocity of ash particles for a total of 76 eruptions from 2014 to 2016 was described as a power law (Figure 4) derived from observed data [33] and previously developed theoretical equations [11,34,48]. The power law formulae obtained in the present study provided the lowest fall velocity for the same diameter, and smaller than with the theoretical equations [34] in which the particle density was assumed to be 2500 (kg m^{-3}).

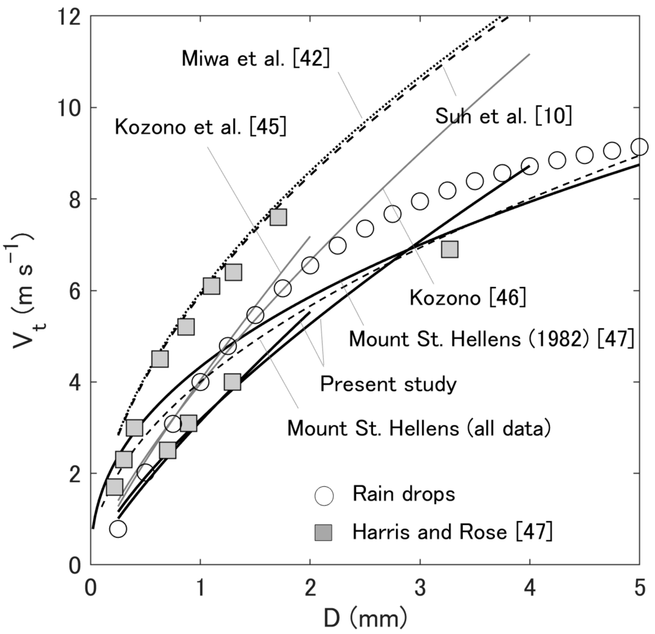

Figure 4. Relationships between ash particle fall velocity and diameter proposed in previous studies and the present one.

4.2. PSD Parameters

4.2.1. Temporal Changes in PSD

Changes in the PSDs of the six selected eruptions over time, as eruption clouds passed over the Parsivel^2 device, are shown in Figure 5. The maximum R_A (11.7 mm h^{-1}) was observed during eruption 4. The number of particles observed per unit volume (N_T) ranged from 10 to 10^3 m^{-3}. R_A and $\log_{10}N_T$ were somewhat correlated. Particles with a maximum diameter of 3.75 mm were observed in eruptions 2b and 3. D_{max} was not necessarily correlated with R_A. In all eruptions except eruption 1, large values of D_{max} were observed immediately after the onset of ash fall (Figure 5). D_{max} and D_m were positively correlated, and D_{max} was negatively correlated with both $\log_{10}N_T$ and $\log_{10} N_w$. These new findings on the PSD of ash particles will be examined in detail in the following sections.

A temporal change in the PSD at a certain point is considered to reflect a spatial change in PSD within the eruption cloud. Therefore, it is necessary to know which part of the eruption cloud was observed by Parsivel^2 when discussing a temporal change in the PSD. The distribution of the time-integrated reflectivity factor in eruption clouds during eruption 6 is shown in Figure 6. We also obtained the trajectories of the centroids of the eruption clouds (data not shown). Calculations of time-integrated radar reflectivity and the trajectories are based on PPI data at an elevation angle of 1.7°. Parsivel^2 data for ash particles in the central part of eruption cloud as it passed over the observation site are shown in Figure 5. Unfortunately, there is no Parsivel^2 site in the area where the accumulated reflectivity factor reached a maximum, since this area is 2 km from the vent and is therefore restricted.

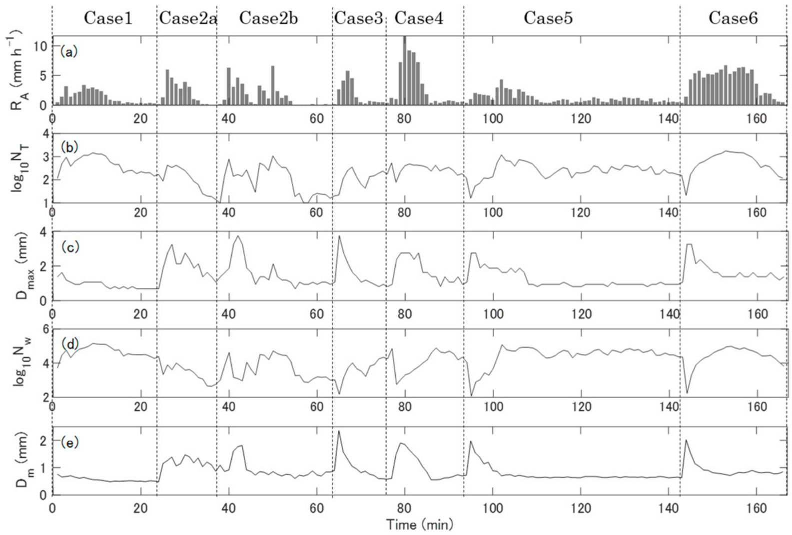

Figure 5. Temporal changes in gamma PSD parameters observed by Parsivel^2 during eruption 6 (16 July 2018). (**a**) Ash fall rate R_A. (**b**) Total number of volcanic ash particles N_T. (**c**) Maximum diameter D_{max}. (**d**) Normalized intercept parameter N_w. (**e**) Mass-weighted diameter D_m.

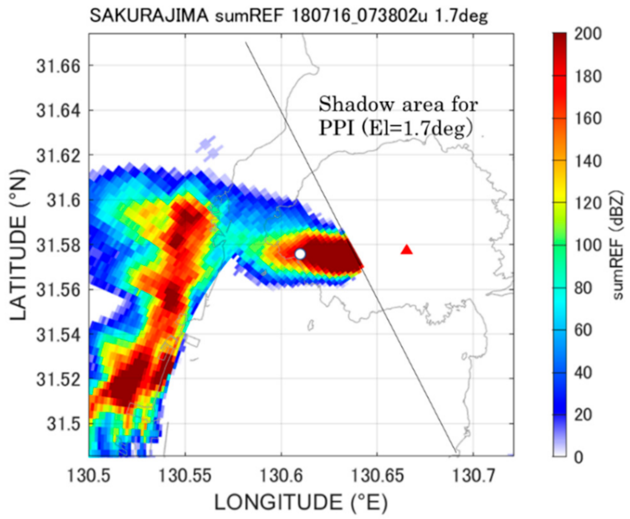

Figure 6. Plan position indicator (PPI) image of time-integrated radar reflectivity for eruption clouds formed in eruption 6 (16 July 2018). PPI images were obtained every 2 min at an elevation angle of 1.7°. Circle indicates the location of Parsivel^2; triangle indicates the summit of Minami-dake.

4.2.2. Gamma PSD Parameters

Temporal changes in the observed PSD profiles for eruption 6 are shown in Figure 7, as a representative example. Two fitting curves of the gamma PSD function are superimposed on each set of observed PSD data; one curve was obtained by the momentum method, and the other curve, by non-linear regression analysis. It should be noted that non-linear regression analysis must be carried out to the logarithmic form of the gamma PSD formula because $N(D)$ distributes over a wide range (from 10^0 to 10^4). A good fit was obtained for all samples, except at 15:54 LST, when large particles were observed. The gamma PSD obtained by the momentum method was approximately exponential, while the gamma PSD obtained by non-linear regression analysis exhibited an upward convex shape that fitted small particles. It should be noted that the results obtained by the two methods employed agree quite well for PSDs at 16:00 LST to 16:04 LST, a period during which only particles smaller than 2 mm were observed. The results suggest that the difference in the gamma PSD functional forms obtained by non-linear regression analysis and the momentum method is acceptable. We analyzed all the PSD data obtained in order to quantitatively confirm the results, which are shown in the discussion section of the present paper.

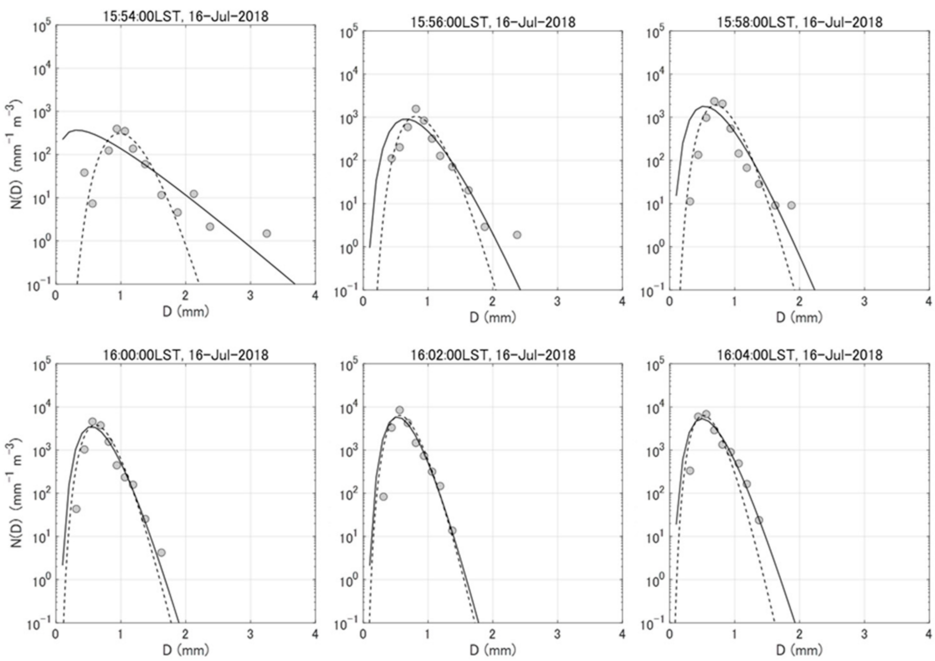

Figure 7. Temporal changes in measured PSD for eruption 6 (16 July 2018). Solid lines and dashed lines are the gamma PDS fitting curves for the measured PSD data by the moment method and non-linear regression analysis, respectively.

To clarify the statistical characteristics of the PSDs of volcanic ash particles, we investigated the frequency distribution and probability density function of four parameters ($\log_{10}N_0$, Λ, D_0, and μ) of gamma PSDs, and of the additional PSD parameters D_{max} and N_T observed in all eruptions. The results are shown in Figure 8. The six parameters ($\log_{10}N_0$, D_0, Λ, μ, D_{max}, and N_T) showed modes (standard deviation [SD]) of 8.8 (9.6), 0.65 (0.29), 13.4 (25.0), 8.3 (13.7), 0.97 (0.679), and 182 (380), respectively. It interesting that each of three parameters ($\log_{10}N_0$, Λ, μ) had a wider range compared with that of precipitation particles. Other descriptive statistics, such as the maximum, median, and skewness, are summarized in Table 4.

Table 4. Statistical values of gamma, normalized, and integrated particle size distribution (PSD) parameters. $\rho_b = 1.25 \times 10^3$ kg m^{-3} and $\rho_p = 2.50 \times 10^3$ kg m^{-3} were assumed for the estimation of R_A.

Parameter	Unit	Mode	Med	Mean	SD	Max	Skew	D_{10}	D_{90}
$\log_{10} N_0$	mm^{-1} m^{-3}	8.83	9.64	15.8	9.64	47.9	0.581	4.79	28.2
L	mm^{-1}	13.4	27.2	33.5	25.0	118	0.742	6.05	65.4
D_0	mm	0.65	0.69	0.79	0.292	2.13	1.88	0.54	1.21
m	–	8.3	17.1	18.9	13.7	67.3	0.661	3.10	36.8
D_{max}	mm	0.97	1.19	1.42	0.679	3.75	1.42	0.81	2.36
$\log_{10}N_w$	mm^{-1} m^{-3}	4.60	4.42	4.15	0.704	5.15	−0.875	3.07	4.87
D_m	mm	0.853	1.19	0.853	0.350	2.36	1.83	0.559	139
N_T	m^{-3}	182	252	381	380	1788	1.75	26	998
R_A	mm h^{-1}	0.52	1.08	2.01	2.17	11.7	1.64	0.23	5.43
C_A	g m^{-3}	0.0931	0.180	0.225	0.189	0.845	1.21	0.0323	0.478
$10\log_{10}Z$	dBZ	17.1	18.2	19.3	7.43	36.9	0.087	9.28	28.8

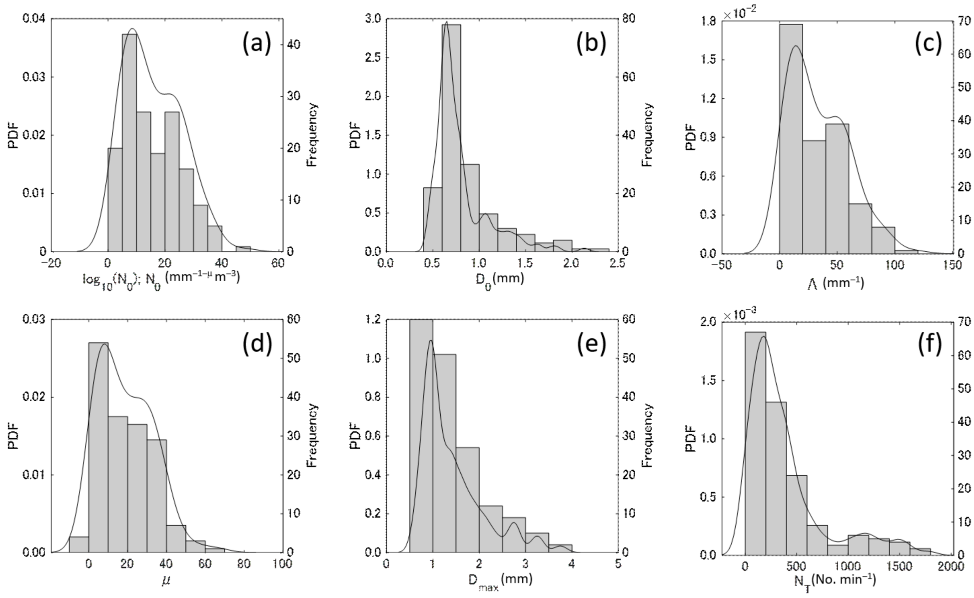

Figure 8. Histogram and probability density function of gamma PSD parameters including the (**a**) log of the intercept parameter ($\log_{10}N_0$), (**b**) median volume diameter (D_0), (**c**) slope parameter (Λ), (**d**) shape parameter (μ), (**e**) maximum particle diameter (D_{max}), and (**f**) total particle number (N_T).

The main objective of radar remote sensing is determining the physical quantities of eruption clouds from measured radar parameters. Normally, the number of physical quantities, which are unknowns, is larger than the number of parameters that can be measured by radar. Therefore, the number of unknowns is reduced by theoretically or empirically defining relationships between unknown parameters. If two parameters are strongly correlated, then the obtained relationship will be incorporated into a weather radar monitoring system for eruption clouds. Theoretical interpretations of such correlations are useful for understanding the microphysical processes of eruption clouds.

Clear correlations were detected between gamma PSD parameters in this study (Figure 9), which suggests that the gamma PSD model well describes the observed volcanic ash PSDs. The relationships between gamma PSD parameters are summarized in Table 5. Thus, if one gamma PSD parameter is obtained, the remaining parameters can be estimated using the information listed in Table 5. A scatter plot of D_{max} and μ is also shown in Figure 9; the shape parameter μ approaches 0 (i.e., exponential PSD) when D_{max} > ~3, and becomes large (i.e., upward concave PSD) when D_{max} is small. Thus, once D_{max} is given for an initial condition of the PSD, μ is determined by the μ–D_{max} relationship. Next, N_0 and Λ are estimated by the N_0–μ and Λ–μ relationships, respectively.

Table 5. Summary of relationships among gamma PSD parameters. The numbers in the brackets are the correlation coefficient and the root-mean-square error, respectively.

	$\log_{10}N_0$	Λ	μ	D_{max}
$\log_{10}N_0$	-	$\log_{10}N_0 = 0.383\,\Lambda + 2.942$ (0.995, 0.91)	$\log_{10}N_0 = 0.684\,\mu + 2.89$ (0.973, 2.211)	$\log_{10}N_0 = 19.67\,D_{max} - 1.606$ (0.920, 3.784)
Λ	$\Lambda = 2.585\log_{10}N_0 - 7.308$ (0.995, 2.361)	-	$\Lambda = 1.751\,\mu + 0.469$ (0.960, 7.005)	$\Lambda = 42.23\,D_{max}^{-2.046}$ (0.937, 8.76)
μ	$\mu = 1.386\log_{10}N_0 - 3.02$ (0.974, 3.148)	$\mu = 0.527\,\Lambda + 1.222$ (0.960, 3.842)	-	$\mu = 23.87\,D_{max}^{-1.713}$ (0.853, 7.178)
D_{max}	$D_{max} = 5.863\log_{10}N_0 - 0.595$ (0.922, 0.263)	$D_{max} = 4.862\,\Lambda^{-0.418}$ (0.937, 0.238)	$D_{max} = 3.018\,\mu^{-0.314}$ (0.779, 0.393)	-

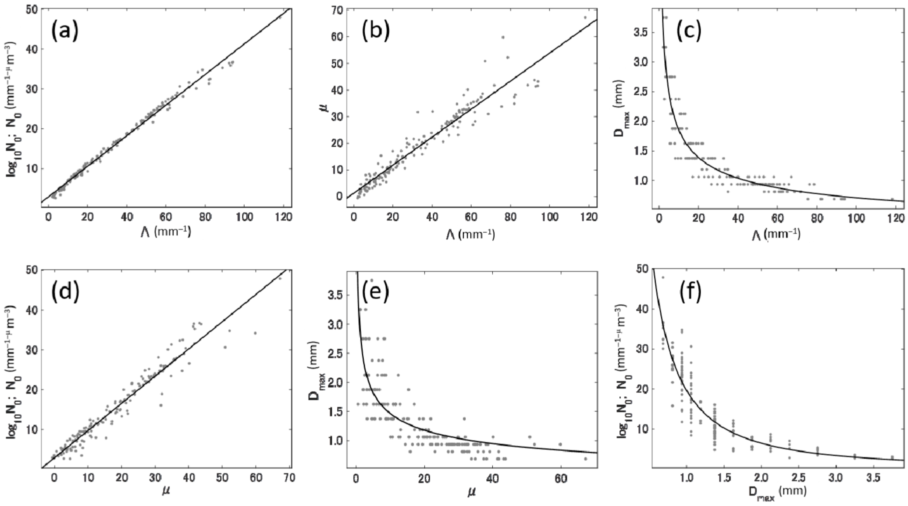

Figure 9. Scatter plots of gamma PSD parameters: (**a**) Λ vs. $\log_{10}N_0$, (**b**) Λ vs. μ, (**c**) Λ vs. $D_{\max}$, (**d**) μ vs. $\log_{10}N_0$, (**e**) μ vs. $D_{\max}$, and (**f**) $D_{\max}$ vs. $\log_{10}N_0$.

4.2.3. Normalized PSD

Figure 10 is a scatter plot showing PSDs before and after normalization. The normalized PSD parameters (N_w and D_m) were calculated directly from the PSD data measured by Parsivel², without assuming a functional form of the PSD. Figure 10a shows the PSD before normalization, which is characterized by wide scattering due to variation in ash fall strength, such that the characteristic distribution could not be observed. After normalization, the PSDs converged to reduce the scatter (Figure 10b), allowing us to observe the form of the distribution. The shape parameter μ was determined by least-squares fitting of the measured $N(D)/N_w$ data according to Equation (23). It may be interesting to examine the associations between N_w or D_m with the type and magnitude of volcanic eruption in a future study, using larger sample sizes.

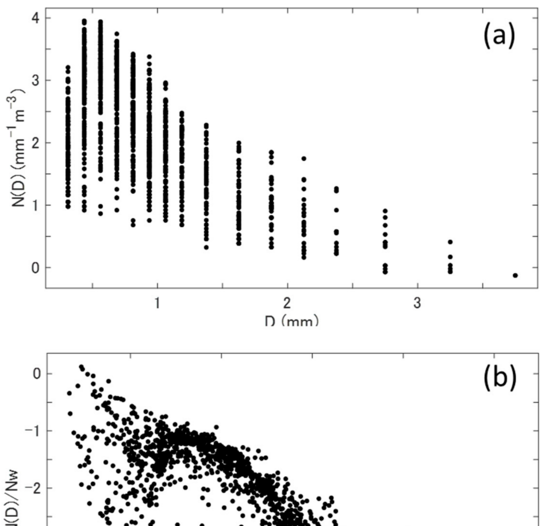

Figure 10. Comparison of PSD before and after normalization: (**a**) $N(D)$ vs. D for the six selected volcanic eruptions measured by Parsivel² and (**b**) corresponding plot of $N(D)/N_w$ vs. D/D_m.

Despite the small sample sizes in the present study, they were useful for determining the statistical characteristics of normalized gamma PSD parameters. Figure 11 shows the frequency distributions and probability density functions of the two parameters (D_m and $\log_{10}N_w$) used to normalize the PSD. The shape parameter μ is shown in Figure 8d. The modes (SD) of D_m and $\log_{10}N_w$ of the normalized gamma PSD parameters were 0.656 (0.350) and 4.60 (0.704), respectively, and the mode (SD) of μ was 8.31 (13.7).

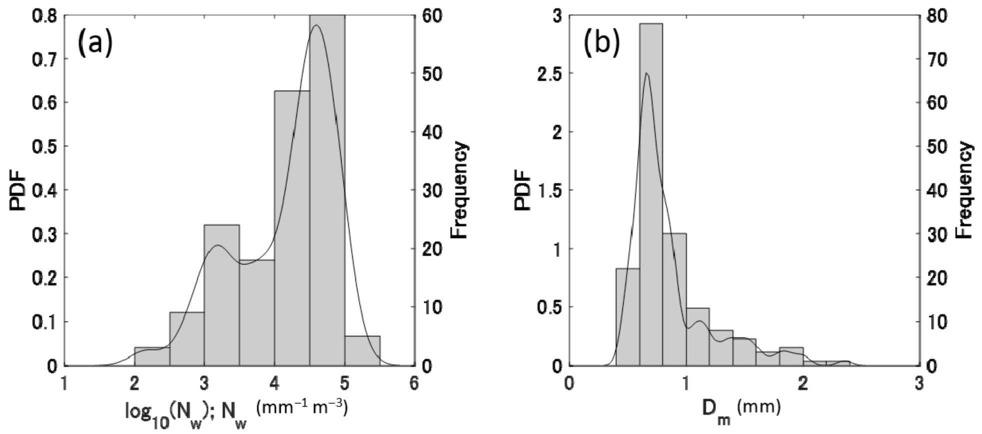

Figure 11. The same as Figure 8, but for normalized PSD parameters including (**a**) $\log_{10}N_w$ and (**b**) D_m.

4.2.4. Quantitative Ash Fall Estimation Using Normalized PSD Parameters

Next, we examined correlations between R_A and gamma PSD parameters (N_w, D_m, and μ). Figure 12 shows a scatter plot of R_A/N_w and D_m. Applying nonlinear regression analysis, we obtained the following power law equation:

$$R_A/N_w = 2.54 \times 10^{-4} {D_m}^{4.97} \tag{42}$$

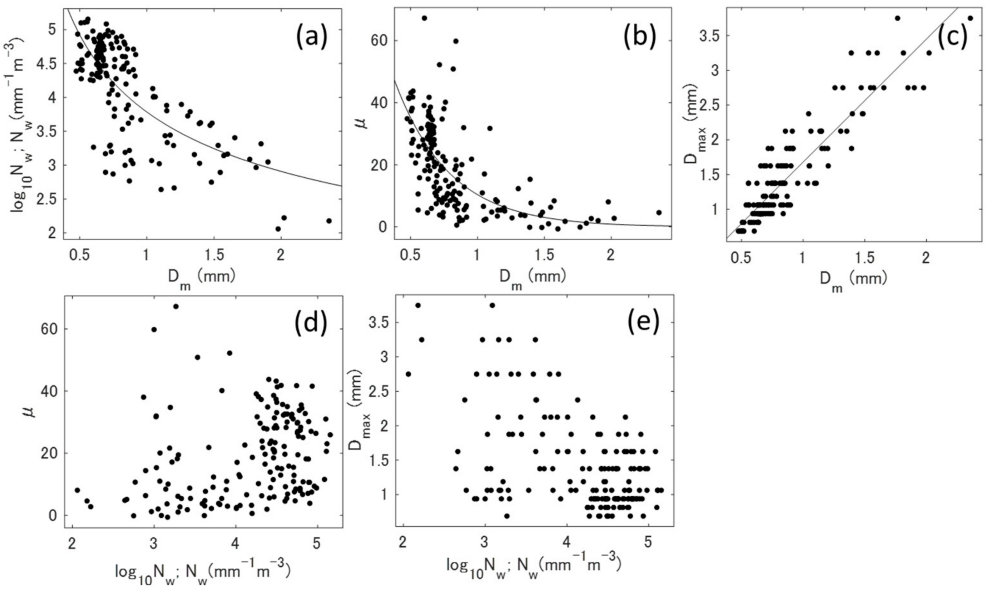

Figure 12. The same as Figure 9, but for normalized PSD parameters including (**a**) D_m vs. $\log_{10}N_w$, (**b**) D_m vs. μ, (**c**) D_m vs. D_{max}, (**d**) $\log_{10}N_w$ vs. μ, and (**e**) $\log_{10}N_w$ vs. D_{max}.

By rearranging Equation (42), we obtained:

$$R_A = 2.54 \times 10^{-4}\, {D_m}^{4.97} N_w \tag{43}$$

The power law equations for the upper and lower 95% confidence limits of Equation (43) are as follows:

$$R_A = 2.72 \times 10^{-4}\, {D_m}^{5.07} N_w;\ \text{95\% upper limit} \quad (44)$$

$$R_A = 2.36 \times 10^{-4}\, {D_m}^{4.87} N_w;\ \text{95\% lower limit} \quad (45)$$

In Figure 12, the correlation coefficient (root-mean-square error) between R_A/N_w and D_m was 0.991 (0.000177), which was higher (lower) than that between R_A and Z, as described in the next section. This result suggests that Equation (42) provides an advanced method for estimating R_A if N_w and D_m are estimated with a sufficient degree of accuracy. For precipitation phenomena, two-frequency radar observations based on satellite remote sensing [49] and dual polarization radar observation [50] have been proposed to estimate N_w and D_m. Similar techniques may be available for ash fall phenomena, and should be explored in a future study.

As physical quantities that represent the microphysical processes within precipitation clouds, $\log N_w$ and D_m have also been used to distinguish precipitation types (stratiform or convective) [51,52]. Similarly, D_m and N_w are expected to provide new insight into volcanic eruption clouds and their microphysical processes in future studies [53–55].

4.3. Conventional Relationship for Quantitative Ash Fall Estimation

Figure 13 shows the frequency and probability density distributions of the three integrated PSD parameters (R_A, C_A, and $10\log_{10}Z$). In this study, the modal values (SD) of R_A, C_A, and $10\log_{10}Z$ of the integrated PSD parameters were 0.52 (2.17), 0.0931 (0.189), and 17.1 (7.48), respectively.

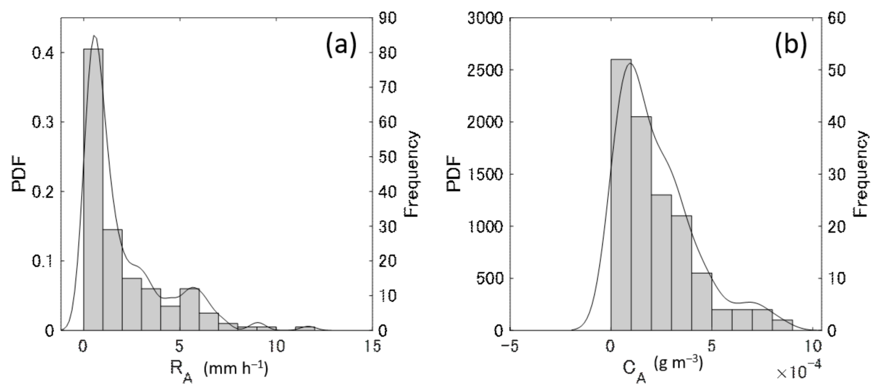

Figure 13. The same as Figure 8, but for integrated PSD parameters including (**a**) R_A and (**b**) C_A.

Next, we investigated the correlations among these integral parameters. In particular, the relationship between R_A and Z is crucial as a practical equation for estimating the R_A from weather radar observations. The C_A–Z relationship is used to estimate the C_A of volcanic ash. These relationships were derived from regression analyses of observed data for each eruption, and are summarized in Table 6. A scatter plot of R_A and Z values obtained from Parsivel^2 observations for all eruptions is shown in Figure 14. The R_A–Z relationship was defined using the nonlinear least-squares method, as follows:

$$R_A = 22.8 \times 10^{-2}\, Z^{0.436};\ R_A\,[\text{mm h}^{-1}],\ Z\,[\text{mm}^6\text{m}^{-3}] \quad (46)$$

The R_A–Z relationships for the upper and lower 95% confidence limits are as follows:

$$R_A = 31.0 \times 10^{-2}\, Z^{0.489};\ \text{95\% upper limit} \quad (47)$$

$$R_A = 14.6 \times 10^{-2}\, Z^{0.383};\ \text{95\% lower limit} \quad (48)$$

It must be mentioned that the R and $RMSE$ for all eruptions are not as good as those of an individual eruption because the PSDs are changeable depending on the eruption case, which is similar to the variation of PSD in precipitation.

Table 6. R_A–Z and C_A–Z relationships obtained from regression analyses of PSD data measured by Parsivel^2. Note that R_A (mm h^{-1}), C_A (g m^{-3}), Z (mm^6 m^{-3}). R: correlation coefficient, $RMSE$: root mean square error. ρ_b = 1.25 × 10^3 kg m^{-3} and ρ_p = 2.50 × 10^3 kg m^{-3} were assumed for the estimation of R_A.

Case	Site	Sampling Period (LST)	(min)	R_A–Z Relationship (R, $RMSE$)	C_A–Z Relationship (R, $RMSE$)	Range
1	NABE	08:22–08:35, 15 May 2018	14	$R_A = 8.62 \times 10^{-2}\ Z^{0.809}$ (0.963, 0.300)	$C_A = 1.51 \times 10^{-2}\ Z^{0.680}$ (0.912, 0.046)	$0 \le Z \le 1 \times 10^2$
2	HART	20:03–20:11, 22 May 2018	9	$R_A = 5.44 \times 10^{-2}\ Z^{0.595}$ (0.910, 0.907)	$C_A = 0.629 \times 10^{-2}\ Z^{0.569}$ (0.950, 0.058)	$0 \le Z \le 2 \times 10^3$
	HIKP	20:00–20:14, 22 May 2018	12	$R_A = 3.03 \times 10^{-2}\ Z^{0.826}$ (0.977, 0.397)	$C_A = 0.496 \times 10^{-2}\ Z^{0.770}$ (0.980, 0.043)	$0 \le Z \le 1 \times 10^3$
3	KURP	08:09–08:13, 30 May 2018	4	$R_A = 14.6 \times 10^{-2}\ Z^{0.522}$ (0.959, 0.613)	$C_A = 1.72 \times 10^{-2}\ Z^{0.423}$ (0.903, 0.055)	$0 \le Z \le 1 \times 10^3$
4	HART	12:03–12:20, 10 June 2018	12	$R_A = 9.45 \times 10^{-2}\ Z^{0.568}$ (0.972, 0.929)	$C_A = 4.49 \times 10^{-2}\ Z^{0.294}$ (0.899, 0.073)	$0 \le Z \le 5 \times 10^3$
5	SBTT	07:35–08:21, 16 June 2018	31	$R_A = 3.55 \times 10^{-2}\ Z^{0.778}$ (0.917, 0.339)	$C_A = 1.20 \times 10^{-2}\ Z^{0.692}$ (0.960, 0.036)	$0 \le Z \le 4 \times 10^2$
6	AKAM	15:53–16:12, 16 July 2018	18	$R_A = 10.0 \times 10^{-2}\ Z^{0.653}$ (0.851, 1.123)	$C_A = 0.553 \times 10^{-2}\ Z^{0.782}$ (0.913, 0.100)	$0 \le Z \le 7 \times 10^2$
All	-	-	88	$R_A = 22.8 \times 10^{-2}\ Z^{0.436}$ (0.819, 1.247)	$C_A = 6.56 \times 10^{-2}\ Z^{0.261}$ (0.634, 0.147)	$0 \le Z \le 5 \times 10^3$

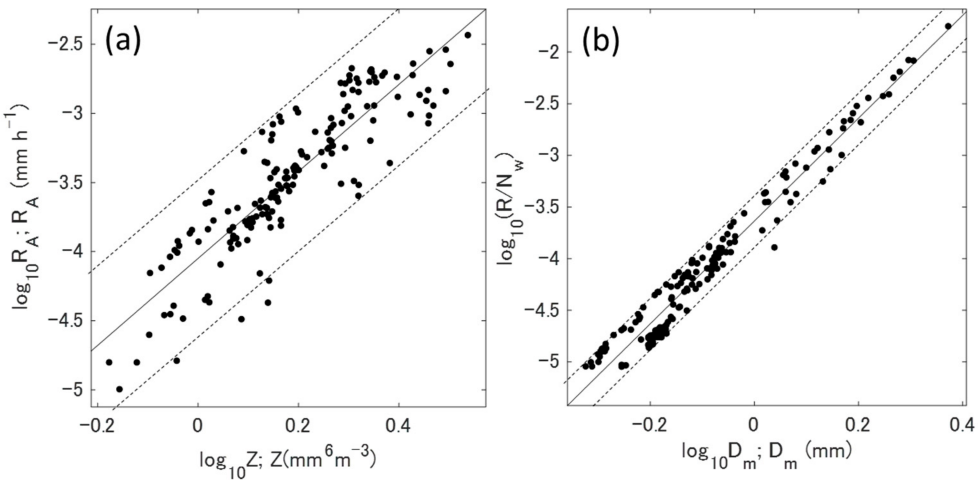

Figure 14. Quantitative ash fall estimation based on the relationships among integrated PSD parameters including (**a**) R_A–Z, (**b**) R_A/N_w–D_m, where R_A, N_w, and D_m were calculated using PSD data obtained by Parsivel^2.

5. Discussion

In radar meteorology, various mathematical formulas for 'precipitation particles' have been proposed by researchers. These include exponential [30], gamma [27,28], log-normal [56,57], Poisson [58], and Weible [59]. The present study assumed a gamma PSD model for 'volcanic ash particles', for the following two reasons. First, gamma PS models have been used widely in previous radar meteorology studies, because the model is relatively simple and its error structure has been investigated [43]. Second, we can compare the results of our analysis with those of previous studies using the same PSD model. The differences in gamma PSD parameters between precipitation particles and volcanic ash particles, if any, can be used to discriminate eruption clouds from precipitation clouds, one of the goals of monitoring volcanic ash falls using radar.

However, when the gamma PSD model is applied to volcanic ash particles, one point remains unclear. 'Does the gamma PSD model represent observed volcanic ash PSD?' This question results from the fact that validation studies have been limited due to the lack of observed ash PSD. In this section, we discuss the validity of the gamma PSD model of volcanic ash using PSD data obtained by Parsivel^2. First, we examined the validity of the momentum method used to calculate the gamma PSD. As we have already shown in Figure 7 in this paper, the gamma $N(D)$ obtained by the momentum method agreed with that obtained by non-linear regression analysis. However, as the number of analyzed PSD samples was limited in Figure 7, we examined all PSD samples obtained in six eruption cases. It should be mentioned again here that non-linear regression analysis must be executed not to $N(D)$ but to $\log_{10}N(D)$. If we used linear $N(D)$ for the analysis, the obtained gamma PSD regression curve would represent only small particles that have large $N(D)$ values. Figure 15 shows comparisons of gamma PSD parameters (N_0, μ, Λ) calculated by the momentum method and non-linear regression analysis. Regression lines obtained were as follows.

$$\mathrm{Log}_{10}\, N_0\_\mathrm{mom} = 0.934 \times \log_{10} N_0\_\mathrm{reg} + 1.47,$$

$$\mu\_\mathrm{mom} = 0.904 \times \mu\_\mathrm{reg} + 2.14,$$

$$\Lambda\_\mathrm{mom} = 0.959 \times \Lambda\_\mathrm{reg} + 2.72.$$

where, the subscripts 'mom' and 'reg' in the variables mean the momentum method and regression analysis, respectively. The correlation coefficient R (the root mean square error $RMSE$) for N_0, μ, and Λ were 0.962 (2.23), 0.940 (4.02), and 0.964 (5.38), respectively. We can confirm from these statistical values that the gamma PSD parameters estimated by the moment method agreed with those obtained by non-linear regression analysis.

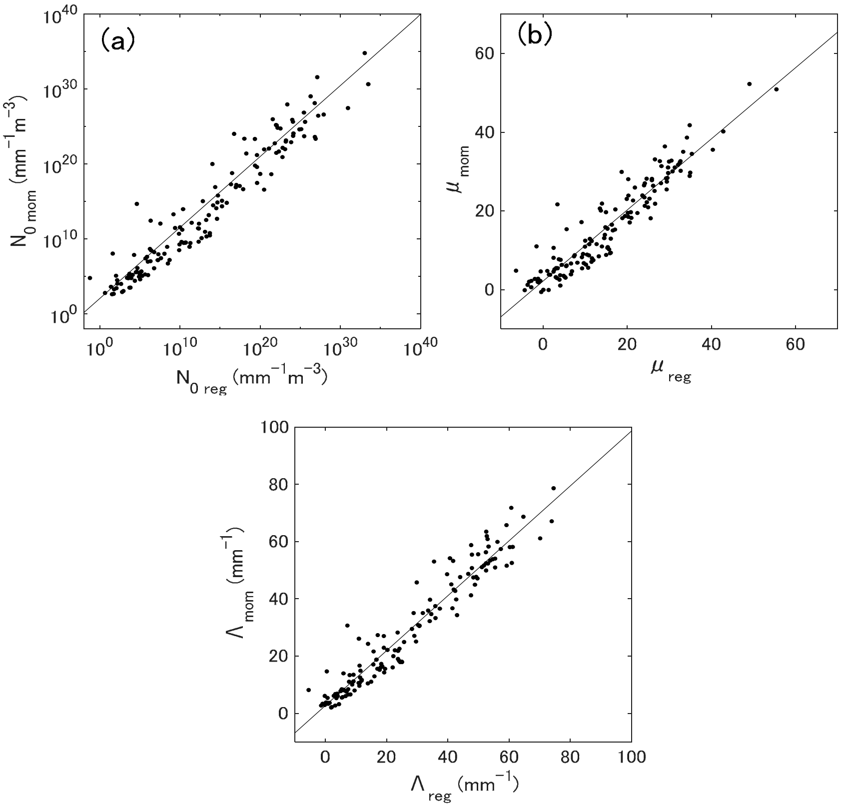

Figure 15. Comparison of gamma PSD parameters obtained from the complete momentum method and non-linear regression analysis. (**a**) log N_0, (**b**) μ, and (**c**) Λ.

Next, we evaluated the validity of the gamma PSD model itself, which is in turn based on the complete momentum method. The result is shown in Figure 16a. Comparing $N(D)$_g based on the gamma model with N (D)_o observed by a Parsivel^2, we obtained N (D)_g = 0.917 × N (D)_o + 0.175. The R and $RMSE$ were 0.825 and 0.554, respectively. According to Figure 16b, most of the residuals of N (D)_g were within ±10% of their values. Given that the value of N (D) ranged from 10^0 to 10^4, these statistical values confirmed that the gamma PSD model is appropriate for describing volcanic ash PSD.

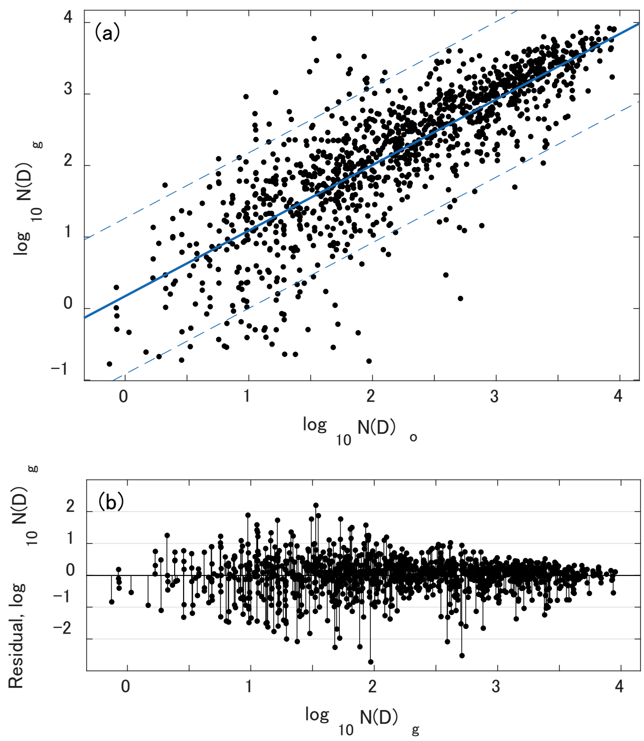

Figure 16. (**a**) Comparison of the gamma PSD model and observed PSDs. The solid line represents the regression line, and the dashed lines are 95% confidence limits. (**b**) The residual of gamma $N(D)$ expressed on a logarithmic scale. The subscripts 'g' and 'o' in the variables mean the gamma PSD model and observed PSD, respectively.

6. Summary

In the present study, we examined the characteristics of the PSD of volcanic ash particles and the relationships among PSD parameters. We used a total of 166 PSD samples collected by Parsivel^2 during six explosive eruptions of the Sakurajima volcano in 2018. The PSD data were analyzed using methods developed for use in radar meteorology.

We proposed gamma and normalized PSD models to describe the PSDs of volcanic ash particles. The observed PSD data were well-described by both models. Strong correlations among the gamma PSD parameters ($\log_{10}N_0$, Λ, and μ) were found and relationships between the gamma PSD parameters were derived. Interestingly, the μ–$R_{\max}$ relationship showed that μ changes inversely with $R_{\max}$. When $D_{\max}$ was large, μ approached zero; i.e., the PSD became exponential. These results could be applied to set up initial PSD conditions for a volcanic ash transport and diffusion model. It must be noted that the range of each of the gamma PSD parameters ($\log_{10}N_0$, Λ, and μ) of ash particles was wider than that of precipitation particles.

The relationships between gamma PSD parameters can be used to solve the inverse problem in radar meteorology, i.e., the retrieval of PSD parameters from weather radar observations. In precipitation studies, D_0 (or Λ) can be estimated from the differential reflectivity Z_{DR}, which is measured by polarimetric radar, and N_0 is estimated from D_0 and observed Z, assuming that μ = 0 [60]. This method is based on the relationship between raindrop shape and diameter, such that flatter raindrops are associated with larger raindrop diameters. Recently, volcanic ash particle shape has been studied using 2DVD, which was designed to measure the shape of a falling raindrop. The classification of ash particle shapes can then be used to identify the volcanic eruption type [61]. To date, a clear relationship between particle shape and diameter has not been found for volcanic ash particles. Further studies of volcanic ash particle shape are required to establish a method for weather radar retrieval of ash particle PSD.

In this study, we also proposed a normalized PSD model, which does not require consideration of the PSD variation associated with ash fall intensity. We found a clear correlation between R_A/N_w and D_m, and derived its power law functional relationship. Once the two parameters N_w and D_m are retrieved from radar measurements, R_A can be estimated from the R_A/N_w–D_m relationship proposed in this study. However, further theoretical and observational studies are needed to retrieve parameters N_w and D_m; for example, scattering simulations based on observed PSD could be used to establish theoretical relationships between N_w and D_m, and polarimetric radar parameters such as Z_{DR} and K_{DP}. Polarimetric radar observations of volcanic ash particles are necessary to validate such theoretical relationships.

Finally, we proposed conventional formulae for estimating the R_A and C_A. The R_A–Z relationship was derived through regression analysis and the C_A–Z relationship was calculated from measured PSD data. Although these relationships have large errors associated with instantaneous monitoring of ash fall caused by spatiotemporal variation in PSD, they are convenient and applicable for radar ash fall monitoring. It should be noted that the relationships obtained in this study were derived from a limited number of data. Thus, further analysis using larger PSD datasets is necessary.

Author Contributions: Conceptualization, M.M.; methodology, M.M.; software, R.T.; validation, M.M. and R.T.; formal analysis, M.M.; investigation, M.M.; resources, M.I.; data curation, M.I.; writing—original draft preparation, M.M.; writing—review and editing, M.M.; visualization, M.M. and R.T.; supervision, M.M.; project administration, M.I.; funding acquisition, M.I. All authors have read and agreed to the published version of the manuscript.

Funding: This research was funded mainly by the Ministry of Education, Culture, Sports, Science and Technology (MEXT) "Integrated Program for Next-generation Volcano Research and Human Resource Development" and partially by the Council for Science, Technology and Innovation (CSTI), "Cross-ministerial Strategic Innovation Promotion Program (SIP)".

Institutional Review Board Statement: Not applicable.

Informed Consent Statement: Not applicable.

Data Availability Statement: Not applicable.

Acknowledgments: This work was supported by the MEXT "Integrated Program for Next-generation Volcano Research and Human Resource Development". The radar data analyzed in the present study were obtained from the Ministry of Land, Infrastructure, Transport and Tourism (MLIT) of Japan using a framework designed by the Data Integration and Analysis System (DIAS), which is funded by MEXT.

Conflicts of Interest: The authors declare no conflict of interest. The funders had no role in the design of the study, the collection, analysis, or interpretation of the data, the writing of the manuscript, or the decision to publish the results.

Glossary

All symbols and units used in the present study are listed below. Conventional units in radar meteorology were used instead of Système international (SI) units.
List of symbols and units used in the present study.

Symbol	Description	Unit
A_i	Effective measured area of the i-th size bin	mm^2
C_A	Volcanic ash mass concentration	$kg\ m^{-3}$
C_{ij}	Number of particles measured in i-th diameter bin and j-th Velocity bin	-
D	Particle diameter	mm
D_0	Median volume diameter	mm
D_m	Mass-weighted mean diameter	mm
D_{max}	Maximum particle diameter	mm
D_{min}	Minimum particle diameter	mm
ΔD_i	Bin size of the i-th diameter channel	mm
$N(D)$	Particle size distribution (PSD)	$mm^{-1}\ m^{-3}$
$N(D_i)$	Number of particles from D_i to $D_i + \Delta D_i$ per unit volume	$mm^{-1}\ m^{-3}$
N_0	Intercept parameter of gamma PSD	$mm^{-1-\mu}\ m^{-3}$
N_T	Total number of volcanic ash particles	m^{-3}
N_w	Normalized intercept parameter of gamma PSD	$mm^{-1}\ m^{-3}$
nd	Number of diameter bins	-
nv	Number of velocity bins	-
R_A	Ash fall rate; 1 ($kg\ m^{-2}h^{-1}$) = ρ_p/ρ_b ($mm\ h^{-1}$)	$mm\ h^{-1}$
Δt	Sampling time (60 s)	s
V_j	Fall velocity measured at the j-th velocity bin	$m\ s^{-1}$
V_t	Fall velocity of a volcanic ash particle	$m\ s^{-1}$
Z	Equivalent reflectivity factor	$mm^6\ m^{-3}$
Λ	Slope parameter of gamma PSD	mm^{-1}
μ	Shape parameter of gamma PSD	-
ρ_b	Bulk density of ash deposits (= $1.25 \times 10^3\ kg\ m^{-3}$)	$kg\ m^{-3}$
ρ_p	Density of a solid ash particle (= $2.5 \times 10^3\ kg\ m^{-3}$)	$kg\ m^{-3}$

References

1. Kaminski, E.; Jaupart, C. The size distribution of pyroclasts and the fragmentation sequence in explosive volcanic eruptions. *J. Geophys. Res.* **1998**, *103*, 29759–29779. [CrossRef]
2. Costa, A.; Pioli, L.; Bonadonna, C. Insights into tephra total grain-size distribution from field data analysis. *Earth Planet. Sci. Lett.* **2016**, *443*, 90–107. [CrossRef]
3. Kueppers, U.; Scheu, B.; Spieler, O. Fragmentation efficiency of explosive volcanic eruptions: A study of experimentally generated pyroclasts. *J. Volcanol. Geoth. Res.* **2006**, *153*, 125–135. [CrossRef]
4. Rust, A.C.; Cashman, K.V. Permeability controls on expansion and size distributions of pyroclasts. *J. Geophys. Res.* **2011**, *116*, B11202. [CrossRef]
5. Cashman, K.V.; Scheu, B. Magmatic fragmentation. In *The Encyclopedia of Volcanoes*, 2nd ed.; Sigurdsson, H., Houghton, B., McNutt, S., Rymer, H., Stix, J., Eds.; Academic Press: Cambridge, MA, USA, 2015; pp. 459–472.
6. Webley, P.; Mastin, L. Improved prediction and tracking of volcanic ash clouds. *J. Volcanol. Geotherm. Res.* **2009**, *186*, 1–9. [CrossRef]
7. Mastin, L.G.; Guffanti, M.; Servranckx, R.; Webley, P.W.; Barsotti, S.; Dean, K.; Denlinger, R.; Durant, A.; Ewert, J.W.; Gardner, C.A.; et al. A multidisciplinary effort to assign realistic source parameters to model of volcanic ash-cloud transport and dispersion during eruptions. *J. Volcanol. Geotherm. Res.* **2009**, *186*, 10–21. [CrossRef]
8. Cashman, K.; Rust, A. Introduction: Part 2: Volcanic ash: Generation and spatial variations. In *Volcanic Ash Hazard Observation*; Mackie, S., Cashman, K., Ricketts, H., Rust, A., Watson, M., Eds.; Elsevier: Amsterdam, The Netherlands, 2016; pp. 5–22.
9. Pioli, L.; Bonadonna, C.; Pistolesi, M. Reliability of total grain-size distribution of tephra deposits. *Sci. Rep.* **2019**, *9*, 10006. [CrossRef]
10. Suh, S.-H.; Maki, M.; Iguchi, M.; Lee, D.-I.; Yamaji, A.; Momotani, T. Free-fall experiments of volcanic ash particles using a 2-D video disdrometer. *Atmos. Meas. Tech.* **2019**, *12*, 5363–5379. [CrossRef]
11. Kozono, T.; Iguchi, M.; Miwa, T.; Maki, M.; Maesaka, T.; Miki, D. Characteristics of tephra fall from eruptions at Sakurajima volcano, revealed by optical disdrometer measurements. *Bull. Volcanol.* **2019**, *81*. [CrossRef]
12. Iguchi, M.; Nakamichi, H.; Tanaka, H.; Ohta, Y.; Shimizu, A.; Miki, D. Integrated monitoring of volcanic ash and forecasting at Sakurajima volcano, Japan. *J. Disast. Res.* **2019**, *14*, 798–809. [CrossRef]
13. Schönhuber, M.; Lammer, G.; Randeu, W.L. The 2D video disdrometer. In *Precipitation: Advances in Measurement, Estimation and Prediction*; Michaelides, S., Ed.; Springer: Berlin/Heidelberg, Germany, 2008; pp. 3–31.
14. Kruger, A.; Krajewski, W.F. Two-dimensional video disdrometer: A description. *J. Atmos. Ocean. Technol.* **2002**, *19*, 602–617. [CrossRef]
15. Löffler-Mang, M.; Joss, J. An optical disdrometer for measuring size and velocity of 852 hydrometeors. *J. Atmos. Ocean. Technol.* **2000**, *17*, 130–139. [CrossRef]

16. Tokay, A.; Wolff, D.B.; Petersen, W.A. Evaluation of the new version of the laser-optical disdrometer, OTT Parsivel^2. *J. Atmos. Ocean. Technol.* **2014**, *31*, 1276–1288. [CrossRef]
17. OTT. *Operating Instructions, Present Weather Sensor, OTT Parsivel^2*; Document Number 70.210.001.B.E 04-0911; Hydromet GmbH: Kempten, Germany, 2011; 46p.
18. Krajewski, W.F.; Kruger, A.; Caracciolo, C.; Golé, P.; Barthes, L.; Creutin, J.-D.; Delahaye, J.-Y.; Nikolopoulos, E.I.; Ogden, F.; Vinson, J.-P. DEVEX—Disdrometer evaluation experiment: Basic results and implications for hydrologic studies. *Adv. Water Resour.* **2006**, *29*, 311–325. [CrossRef]
19. Lanza, L.G.; Vuerich, E. The WMO field intercomparison of rain intensity gauges. *Atmos. Res.* **2009**, *94*, 534–543. [CrossRef]
20. Thurai, M.; Petersen, W.A.; Tokay, A.; Schultz, C.; Gatlin, P. Drop size distribution comparisons between Parsivel and 2-D video disdrometers. *Adv. Geosci.* **2011**, *30*, 3–9. [CrossRef]
21. Joss, J.; Waldvogel, A. Ein spektrograph für niederschlagstropfen mit automatischer auswertung (A spectrograph for raindrops with automatic interpretation). *Pure Appl. Geophys.* **1967**, *68*, 240–246. [CrossRef]
22. Kagoshima Local Meteorological Observatory, 2019. List of Sakurajima Eruptions in 2013. Available online: https://www.jma-net.go.jp/kagoshima/vol/data/skr_exp_list/skr_exp_2019.html (accessed on 23 April 2021). (In Japanese)
23. JMA. Available online: https://www.jma-net.go.jp/kagoshima/vol/data/skr_exp_2013.html (accessed on 3 October 2019).
24. Maki, M.; Kim, Y.; Kobori, T.; Hirano, K.; Lee, D.-I.; Iguchi, M. Analyses of three-dimensional weather radar data from volcanic eruption clouds. *J. Volcanol. Geotherm. Res.* **2021**. [CrossRef]
25. DIAS. XRAIN Precipitation Original Data search and Download System. Available online: https://auth.diasjp.net/cas/login?service=http://xrain.diasjp.net/original/&locale=en (accessed on 13 March 2019).
26. Guyot, A.; Pudashine, J.; Protat, A.; Uijlenhoet, R.; Pauwels, V.R.N.; Seed, A.; Walker, J.P. Effect of disdrometer type on rain drop size distribution characterisation: A new dataset for south-eastern Australia. *Hydrol. Earth Syst. Sci.* **2019**, *23*, 4737–4761. [CrossRef]
27. Ulbrich, C.W. Natural variations in the analytical form of the drop size distribution. *J. Clim. Appl. Meteorol.* **1983**, *22*, 1764–1775. [CrossRef]
28. Ulbrich, C.W.; Atlas, D. Assessment of the contribution of differential polarization to improved rainfall measurements. *Radio Sci.* **1984**, *19*, 49–57. [CrossRef]
29. Chandrasekar, V.; Bringi, V.N. Simulation of radar reflectivity and surface measurements of rainfall. *J. Atmos. Ocean. Technol.* **1987**, *4*, 464–478. [CrossRef]
30. Marshall, J.S.; Palmer, W.M. The distribution of raindrops with size. *J. Meteorol.* **1948**, *5*, 165–166. [CrossRef]
31. Miwa, T.; Maki, M.; Kozono, T.; Fujita, E.; Tanada, T.; Iguchi, M. Experimental measurement on falling velocity of volcanic ash from Sakurajima volcano by using PARSIVEL disdrometer. *Annu. Disas. Prev. Res. Inst. Kyoto Univ.* **2015**, *58*, 91–94. Available online: http://hdl.handle.net/2433/210085 (accessed on 23 April 2021). (In Japanese with English abstract).
32. Kozono, T.; Miwa, T.; Maki, M.; Maesaka, T.; Miki, D.; Iguchi, M. PARSIVEL tephra-fall observations at Sakurajima Volcano. *Annu. Disast. Prev. Res. Inst. Kyoto Univ.* **2015**, *58B*, 86–90, (In Japanese with English abstract). Available online: http://hdl.handle.net/2433/210086 (accessed on 23 April 2021). (In Japanese with English abstract).
33. Kozono, T.; Tohoku University, Sendai, Miyagi, Japan. Personal communication, 2020.
34. Harris, D.M.; Rose, W.I. Estimating particle sizes, concentrations, and total mass of ash in volcanic clouds using weather radar. *JGR Oceans* **2019**, *88*, 10969–10983. [CrossRef]
35. Sekhon, R.S.; Srivastava, R.C. Doppler radar observations of drop-size distributions in a thunderstorm. *J. Atmos. Sci.* **1971**, *28*, 983–994. [CrossRef]
36. Willis, P.T. Functional fits to some observed drop size distributions and parameterization of rain. *J. Atmos. Sci.* **1984**, *41*, 1648–1661. [CrossRef]
37. Sempere Torres, D.; Porrà, J.M.; Creutin, J.-D. 1998: A general formulation for raindrop size distribution. *J. Geophys. Res.* **1998**, *103*, 1785–1797. [CrossRef]
38. Testud, J.; Le Bouar, E.; Obligis, E.; Ali Mehenni, M. The rain profiling algorithm applied to polarimetric weather radar. *J. Atmos. Ocean. Technol.* **2000**, *17*, 332–356. [CrossRef]
39. Testud, J.; Oury, S.; Black, R.A.; Amayenc, P.; Dou, X. The concept of "normalized" distribution to describe raindrop spectra: A tool for cloud physics and cloud remote sensing. *J. Appl. Meteorol.* **2001**, *40*, 1118–1140. [CrossRef]
40. Delanoë, J.; Protat, A.; Testud, J.; Bouniol, D.; Heymsfield, A.J.; Bansemer, A.; Brown, P.R.A.; Forbes, R.M. Statistical properties of the normalized ice particle size distribution. *J. Geophys. Res.* **2005**, *110*, D10201. [CrossRef]
41. Kozu, T.; Nakamura, K. Rainfall parameter estimation from dual-radar measurements combining reflectivity profile and path-integrated attenuation. *J. Atmos. Ocean. Technol.* **1991**, *8*, 251–271. [CrossRef]
42. Ulbrich, C.W.; Atlas, D. Rainfall microphysics and radar properties: Analysis methods for drop size spectra. *J. Appl. Meteorol.* **1998**, *37*, 912–923. [CrossRef]
43. Ulbrich, C.W. The effects of drop size distribution truncation on rainfall integral parameters and empirical relations. *J. Climate Appl. Meteorol.* **1985**, *24*, 580–590. [CrossRef]
44. Sekhon, R.S.; Srivastava, R.C. Snow size spectra and radar reflectivity. *J. Atmos. Sci.* **1970**, *28*, 983–994. [CrossRef]

45. Bagheri, G.; Bonadonna, C. Aerodynamics of volcanic particles: Characterization of size, shape, and settling velocity. In *Volcanic Ash Hazard Observation*; Mackie, S., Cashman, K., Ricketts, H., Rust, A., Watson, M., Eds.; Elsevier: Amsterdam, The Netherlands, 2016; pp. 39–52. [CrossRef]
46. Manzella, I.; Bonadonna, C.; Phillips, J.C.; Monnard, H. The role of gravitational instabilities in deposition of volcanic ash. *Geology* **2015**, *43*, 211–214. [CrossRef]
47. Freret-Lorgeril, V.; Gilchri, J.; Donnadieu, F.; Jellinek, A.M.; Delanoë, J.; Latchimy, T.; Vinson, J.P.; Caudoux, C.; Peyrin, F.; Hervier, C.; et al. Ash sedimentation by fingering and sediment thermals from wind-affected volcanic plumes. *Earth Planet. Sci. Lett.* **2020**, *534*. [CrossRef]
48. Ganser, G.H. A rational approach to drag prediction of spherical and nonspherical particles. *Powder Technol.* **1993**, *77*, 143–152. [CrossRef]
49. Liao, L.; Meneghini, R.; Iguchi, T.; Tokay, A. Characteristics of DSD bulk parameters: Implication for radar rain retrieval. *Atmosphere* **2020**, *11*, 670. [CrossRef]
50. Bringi, V.; Chandrasekar, V. *Polarimetric Doppler Weather Radar: Principles and Applications*; Cambridge University Press: Cambridge, UK, 2001; pp. 378–426. [CrossRef]
51. Bringi, V.N.; Chandrasekar, V.; Hubbert, J.; Gorgucci, E.; Randeu, W.L.; Schoenhuber, M. Raindrop size distribution in different climatic regimes from disdrometer and dual-polarized radar analysis. *J. Atmos. Sci.* **2003**, *60*, 354–365. [CrossRef]
52. Jayalakshmi, J.; Seela, B.K.; Lin, P.-L.; Wang, P.K.; Tseng, C.-H.; Reddy, K.K.; Hashiguchi, H.; Feng, L.; Das, S.K.; Unnikrishnan, C.K. Raindrop size distribution characteristics of Indian and Pacific Ocean tropical cyclones observed at India and Taiwan sites. *J. Meteorol. Soc. Japan* **2020**, *98*, 299–317. [CrossRef]
53. Coata, A.; Folch, A.; Macedonio, G. A model for wet aggregation of ash particles in volcanic plumes and clouds: 1. Theoretical formulation. *J. Geophys. Res.* **2010**, *115*, B09201. [CrossRef]
54. Folch, A.; Costa, A.; Durant, A.; Macedonio, G. A model for wet aggregation of ash particles in volcanic plumes and clouds: 2. Model application. *J. Geophys. Res.* **2010**, *115*, B09202. [CrossRef]
55. Brown, R.J.; Bonadonna, C.; Durant, A.J. A review of volcanic ash aggregation. *Phys. Chem. Earth Parts A/B/C* **2012**, *45–46*, 65–78. [CrossRef]
56. Markowitz, A.H. Raindrop size distribution experiments. *J. Appl. Meteorol.* **1976**, *15*, 1029–1166. [CrossRef]
57. Feingold, G.; Levin, Z. Application of the lognormal rain-drop distribution to differential reflectivity radar measurements (ZDR). *J. Atmos. Ocean. Technol.* **1987**, *4*, 377–382. [CrossRef]
58. Cornford, S.G. Sampling errors in measurements of raindrop and cloud droplet concentrations. *Meteorol. Mag.* **1967**, *96*, 271–282.
59. Best, A. The size distribution of raindrops. *Quart. J. Roy. Meteorol. Soc.* **1950**, *76*, 16–36. [CrossRef]
60. Seliga, T.A.; Bringi, V.N. Potential use of radar differential reflectivity measurements at orthogonal polarizations for measuring precipitation. *J. Appl. Meteorol.* **1976**, *15*, 69–76. [CrossRef]
61. Shoji, D.; Noguchi, R.; Otsuki, S.; Hino, H. Classification of volcanic ash particles using a convolutional neural network and probability. *Sci. Rep.* **2018**, *8*, 8111. [CrossRef]